

RESEARCH ARTICLE | JANUARY 13 2023

Experimental investigation of film reversal evolution characteristics in gas–liquid annular flow

Li-song Wang (王黎松) ; Meng Yang (杨猛) ; Lin-tong Hou (侯林彤) ; Shuo Liu (刘硕)  ; Jian Zhang (张健) ; Jing-yu Xu (许晶禹)  

 Check for updates

AIP Advances 13, 015013 (2023)


<https://doi.org/10.1063/5.0135777>



View Online




Export Citation



APL Machine Learning

2023 Papers with Best Practices in Data Sharing and Comprehensive Background

[Read Now](#)



Experimental investigation of film reversal evolution characteristics in gas–liquid annular flow

Cite as: AIP Advances 13, 015013 (2023); doi: 10.1063/5.0135777
Submitted: 23 November 2022 • Accepted: 29 December 2022 •
Published Online: 13 January 2023



View Online



Export Citation



CrossMark

Li-song Wang (王黎松),^{1,2} Meng Yang (杨猛),^{1,2} Lin-tong Hou (侯林彤),^{1,2} Shuo Liu (刘硕),^{1,2,a)}
Jian Zhang (张健),^{1,2} and Jing-yu Xu (许晶禹)^{1,2,a)}

AFFILIATIONS

¹School of Engineering Sciences, University of Chinese Academy of Sciences, Beijing 100049, China

²Institute of Mechanics, Chinese Academy of Sciences, Beijing 100190, China

^{a)}Authors to whom correspondence should be addressed: liushuo@imech.ac.cn and xujingyu@imech.ac.cn

ABSTRACT

In natural gas wells, liquid loading is a severe problem threatening production safety. Published studies have verified that liquid loading is closely related to film reversal in gas–liquid annular flow, but the evolution of the film reversal is still unclear. This article reports on experiments conducted to reveal the film reversal evolution characteristics. Experiments were conducted in a 50-mm-diameter vertical pipe with superficial gas velocities ranging from 5.66 to 22.64 m/s and superficial liquid velocities ranging from 0.014 to 0.170 m/s. A camera and electrical resistance tomography were used to obtain qualitative and quantitative results, and an error analysis verified the experiments' repeatability and reliability. The evolution process is divided objectively into three stages to clarify the film reversal: no film reversal (No-FR), the onset of film reversal (Onset-FR), and complete film reversal (Complete-FR). The three stages occur successively with decreasing gas velocity. The characteristics of the individual stages are elaborated, including the interfacial structures, morphological features, and motion trajectories. The void fractions are analyzed in both the time and frequency domains, where the statistical parameters of the probability density function, average value, and standard deviation are presented. The results show that the Onset-FR stage exhibits characteristics similar to both the No-FR and Complete-FR stages, indicating that it plays an intermediate role in the gradual evolutionary process. The current experimental results also achieve excellent agreement with published datasets and correlations.

© 2023 Author(s). All article content, except where otherwise noted, is licensed under a Creative Commons Attribution (CC BY) license (<http://creativecommons.org/licenses/by/4.0/>). <https://doi.org/10.1063/5.0135777>

I. INTRODUCTION

Annular flow is an important flow regime in gas–liquid two-phase flows, and its morphology is characterized by a continuous liquid film on the pipe wall, a continuous gas core at the pipe center, and entrained droplets in the gas core (Hewitt and Hall-Taylor, 1970; Kumar *et al.*, 2016). Both gas and liquid phases flow upward at high speeds in concurrent annular flow. However, if the gas velocity is reduced to a specific value, the liquid phase (liquid film or droplets) changes to a downward flow because of gravity. This change in direction from upward to downward has spurred researchers' interest for many years because it is widely encountered in many industrial processes (Govan *et al.*, 1991; Barbosa *et al.*, 2016; and Luan and Vemuri, 2000).

In natural gas exploitation wells, the flow reversal has been treated as the root cause of liquid loading, creating a severe problem during the natural gas exploitation process. In the early stages of a natural gas production well, the upward gas velocity is relatively high, and the flow regime is annular. In this case, the liquid phase on the well bottom can be lifted to the ground level. However, in a gas well's later stages, the gas velocity may be insufficient to carry the liquid phase to the ground level. In this case, a flow reversal occurs, causing liquid accumulation in the well bottom (Turner *et al.*, 1969) and resulting in a remarkable production rate decline.

Various mathematical models have been proposed based on different mechanisms to predict liquid loading behavior. The liquid phase exits in two forms: entrained droplets and liquid film. Hence,

there are two mechanisms to explain the reasons for liquid loading: droplet reversal and film reversal.

The droplet reversal mechanism means that liquid loading occurs when the gas velocity is insufficient to lift the largest droplet. [Turner et al. \(1969\)](#) developed a droplet reversal model to predict the critical gas velocity when the largest droplet begins flowing downward. Later, several modifications were developed by different researchers to improve the droplet model's performance. [Coleman et al. \(1991\)](#) modified the [Turner et al. \(1969\)](#) model and applied it to low-pressure wells. The droplet reversal model by [Nosseir et al. \(2000\)](#) considered different flow conditions and regimes. Using the minimum gas velocity concept by [Turner et al. \(1969\)](#), [Guo et al. \(2006\)](#) proposed a minimum kinetic energy model to predict loaded wells. [Belfroid et al. \(2008\)](#) proposed a correlation introducing the inclination angle to the droplet model. Because these droplet reversal models are accurate and easy to use, they have been widely applied to natural gas wells.

However, in recent years, many investigators have questioned the droplet reversal mechanism's validity because some laboratory experiments showed that the film reversal concept could be more reliable than droplet reversal. [van't Westende et al. \(2007\)](#) studied droplet sizes in a vertical 50-mm-diameter pipe. Their results showed that droplet reversal does not happen, indicating that droplet assumption in [Turner et al. \(1969\)](#) may not be the liquid loading mechanism. In addition, many studies have shown that liquid loading occurs under film reversal conditions rather than droplet reversal ([Veeken et al., 2009](#); [Guner et al., 2015](#)). Therefore, the film reversal mechanism has gained importance recently.

The film reversal mechanism means that the downflow of the liquid film leads to liquid loading. [Hewitt and Hall-Taylor \(1970\)](#) suggested that liquid film downflow occurs when the gas velocity is reduced in annular flow. Two correlations from [Wallis \(1969\)](#) and [Pushkina and Sorokin \(1969\)](#) were proposed to predict film downflow in various pipe sizes ([Wallis and Makkenchery, 1974](#)). [Taitel et al. \(1982\)](#) established a film model based on the mechanical equilibrium of a liquid film. By analyzing the forces, they proposed that the film reversal occurs when the interfacial shear reaches a minimum, corresponding to the critical condition when the liquid film becomes unstable. [Barnea \(1986\)](#) developed a film reversal model to predict the transition from annular to intermittent flow using stability analysis. Later, numerous models were developed by modifying the [Barnea \(1986\)](#) model to improve its capability in vertical and inclined pipes ([Luo et al., 2014](#); [Wang et al., 2022](#)). These theoretical studies provided effective approaches to estimating liquid loading.

In addition to mechanistic models, film reversal experiments are crucial to understanding their physical behavior. [Hewitt \(1985\)](#) studied flow reversal in annular flow and found a falling film with significant interfacial structures of flooding waves. He reported that the occurrence of this falling film is related to the minimum pressure gradient. [Park and Mudawar \(2013\)](#) and [Barbosa et al. \(2016\)](#) investigated the film reversal of condensation in vertical and inclined small pipes. It was found that [Wallis \(1969\)](#) correlation agreed well with the experiments.

[Waltrich et al. \(2015\)](#) conducted experiments in a long vertical pipe with a 42 m height and 0.048 m diameter to investigate the transition from annular to churn flow. A reversal of the liquid film was observed in churn flow, and a large film front with oscillatory behavior appeared when churn flow was developing. [Guner et al. \(2015\)](#)

observed a reversal process by observing entrained bubbles in the liquid film. They found that the bubbles stagnate at low gas velocity until they meet large upward waves. These experiments help to understand some physical features of film reversal.

Although the preceding literature review shows that significant research studies have been conducted to estimate or understand film reversal, few studies focused on the evolution process of film reversal. It should be noted that the film reversal is not a steady concept but a transient process that happens with decreasing gas velocity. During the reversal process, the flow behavior is relatively complicated because it involves the direction change of liquid phase, as well as chaotically interfacial structures on the liquid film. Hence, it is crucial to understand the physical phenomena during the reversal process and investigate the evolution characteristics.

The current work aims to shed light on this problem by investigating the evolution characteristics of film reversal using visualization and tomography, providing new qualitative and quantitative results to better understand how the film reverses. Experiments were carried out in vertical pipes of 50 mm diameter. A camera and electrical resistance tomography (ERT) were adopted as the measuring techniques described in Sec. II. Then, the experimental results, discussion, and comparison with published studies are presented in Sec. III. Finally, Sec. IV summarizes the conclusions from this study.

II. LABORATORY EXPERIMENT

A. Flow loop

As shown in [Fig. 1](#), the flow loop consists of a test section, measuring devices, and supply systems. The test section is a 3.5 m long vertical circular pipe made of transparent plexiglass for visual observation, with a 50 mm inner diameter and a 10 mm wall thickness. The pipe length is 70 times the pipe diameter, suitable for forming a fully developed annular flow. A gas and liquid mixture inlet

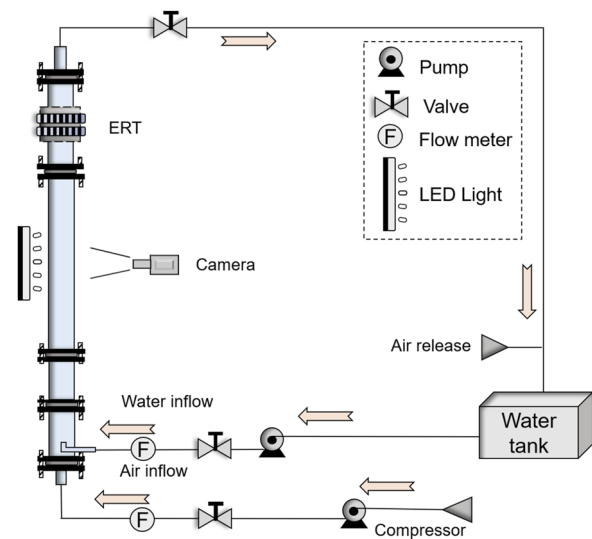


FIG. 1. Schematic of the flow loop.

section at the bottom of the vertical pipe formed the concurrent annular flow. Air and tap water were used as the gas and liquid phases, respectively. A water pump supplied water from a tank, and the air was pressurized by a screw air pump. At the end of the test pipe, the gas and liquid mixture flowed out, with the air eventually released into the atmosphere and the water flowing back to the tank.

Twenty-eight experiments were conducted at different gas and liquid velocities. The superficial gas velocities were 22.64, 19.81, 16.98, 14.15, 11.32, 8.49, and 5.66 m/s, corresponding to superficial gas Reynolds numbers ranging from 19 000 to 76 000. The superficial liquid velocities were 0.014, 0.042, 0.085, and 0.170 m/s, corresponding to superficial liquid Reynolds numbers ranging from 700 to 8500. The film reversal is produced by decreasing the gas velocity from 22.64 to 5.66 m/s.

A turbine flowmeter with a range of 0.1–1.2 m³/h measured the liquid-phase volumetric flow rate. The precision of the turbine flowmeter is 0.5%, so the maximum uncertainty is ± 0.006 m³/h. A rotameter with a 20–160 m³/h range was used for the gas phase. The rotameter has a precision of 1.5%, corresponding to a maximum uncertainty of ± 2.4 m³/h. A camera recorded high-resolution pictures and videos, and electrical resistance tomography (ERT) was adopted to visualize the interior structure of annular flow and measure the void fractions.

B. Instruments

1. Camera

A PENTAX K-50 digital single-lens reflex camera recorded the videos and images. As presented in Fig. 1, the camera was positioned in front of the transparent pipe. A long observation section was located 1 m above the inlet section, allowing an axial length of 45 cm to be observed and making it possible to capture the axial flow evolution. A LED shadowless lamp was positioned behind the transparent pipe to provide sufficient light. The LED light has the advantages of high quality and uniform illumination, so different interfacial structures could be discriminated easily. The video mode was set to 30 frames per second (fps). The photo mode was set at a shutter speed of 1/6000 s to obtain high-resolution photographs to observe the interfacial structures clearly.

2. Electrical resistance tomography (ERT)

A dual-plane electrical resistance tomography instrument was used to study the flow structures and void fractions. Compared with other multiphase measuring technologies, such as wire mesh sensors (WMS) and conductivity probes, a primary advantage of ERT is that it employs non-immersion technology so that the cross-sectional phase distribution can be detected without disturbing the interior flow (Liu *et al.*, 2022). Figure 2(a) is a schematic of the ERT device. Its inner diameter is the same as that of the flow pipe, i.e., 50 mm. The whole ERT working system is shown schematically in Fig. 2(b), including an ERT device, a data acquisition system, and post-processing software. It can be seen that there are two measuring planes in the ERT device. Each measuring plane consists of 16 electrodes, which are uniformly embedded in the pipe wall. These electrodes are non-intrusive so that the flow domain would not be disturbed. The electrodes have two functions: injecting current and measuring voltage (Jia *et al.*, 2010; Wang, 2015). The electronic signals are transferred to an acquisition system (EIT-8000)

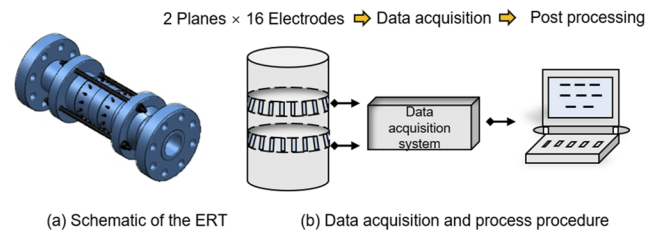


FIG. 2. Schematic of the ERT device and the data acquisition system.

and post-processed by the commercial software MFVAS (Multi-phase Flow Visualization and Analysis System). Finally, the whole ERT system outputs the phase distribution of each measuring plane. This working procedure of ERT is briefly presented here since this paper focuses on the film reversal. One could find detailed working principles of ERT in the study by Wang (2015).

At each test condition, the ERT was sampled for 35.83 s at a sampling rate of 1.493 ms/frame, totaling 24 000 frames. The sampling time and frequency are sufficient to obtain the qualitative and quantitative information of interest. The ERT system must be calibrated to obtain reliable tomography results. The pipe was filled with water before each experiment. Then, the standing water was sampled to check the ERT's repeatability and reliability. The results showed that the relative error between each sampling frame is $< 2\%$, so the sampling results are repeatable. An accurate measurement of the void fraction for pure water should be zero. The results showed that the maximum calibrated void fraction is 0.002, which is relatively low and acceptable considering that tap water may contain microbubbles. These operations reduced the possibility of systematic errors in this work.

C. Experimental uncertainties and error analysis

Experimental uncertainties may be attributed to systematic and random errors (Bevington and Robinson, 2003). In this work, the systematic errors were mainly caused by the instruments. The uncertainties of individual devices and the methods used to mitigate them have been described in Sec. II B. Multiple experiments were conducted to calculate the random errors and assess the experimental repeatability. The accuracy of the current experiments was evaluated by comparing the measured void fractions with published models. The details of these uncertainties and error analysis are presented in Sec. III E 1, which demonstrates that the current experiments are repeatable.

III. RESULTS AND DISCUSSION

A. Evolution stages during the film reversal

The goal of this work is to investigate the evolution of film reversal. Notably, a challenge to clarifying this evolution is to describe the relatively chaotic phenomenon during film reversal. Therefore, to describe the complicated film reversal with clear steps, a new discrimination procedure will be developed in this work, which objectively divides the evolution process into three stages: no flow reversal (No-FR), the onset of flow reversal (Onset-FR), and complete flow reversal (Complete-FR). According to visual observations, the three stages occur successively with decreasing gas

velocity and are discriminated by the interfacial structures and their motion trajectories. The characteristics of the interfacial structures are presented in Secs. III B and III C.

B. Interfacial structures

Figure 3 shows the interfacial structures for a superficial liquid velocity of 0.014 m/s. In Figs. 3(a)–3(c), where the superficial gas velocities exceed 16.98 m/s, the LED light is sufficient to penetrate the transparent tube, indicating that the liquid film is relatively thin and smooth. Previous experiments have shown that there are two types of wavy structures in annular flow: disturbance waves and ripples (Alekseenko *et al.*, 2009; Wang *et al.*, 2021). It can be seen that disturbance waves existing on the thin film are easily recognized because of the large size and the circumferential distribution. In addition, the thin film is covered by many small waves called ripples. It is apparent that a small individual ripple is not coherent circumferentially. The sizes of the disturbance waves and ripples increase gradually with decreasing gas velocity. By combining the video recording, which will be presented in Subsection III C, it is observed that all ripples and disturbance waves flow upward at relatively high speeds. Hence, Figs. 3(a)–3(c) can be recognized as No-FR because no downward movement happens.

Onset-FR occurs when the gas velocities decrease to 14.15 and 11.32 m/s, as shown in Figs. 3(d) and 3(e). The main reason for classifying these two flow conditions as Onset-FR is that the interfacial waves exhibit stagnation, as presented in Sec. III C. In Figs. 3(d) and 3(e), the film has many wrinkles corresponding to ripples. Additionally, huge waves appear that are larger than the disturbance waves.

Here, the term “huge wave” is used, considering that Onset-FR is an aspect of churn flow. In churn flow, the term “huge wave” is generally used to describe large-scale waves (Sekoguchi and Takeishi, 1989). Using WMS, Parsi *et al.* (2015) suggested that the huge wave structure could occur in two forms. One form exists with a continuous gas core encircled by a large wave, and another occurs with an agitated gas and liquid mixture core. And, with the

increasing gas velocity, the former would become dominant. Figures 3(d) and 3(e) agree with the former description by Parsi *et al.* (2015) because it can be observed that the gas core is continuous.

With a further decrease in the gas velocity to 8.49 and 5.66 m/s, Complete-FR occurs in Figs. 3(f) and 3(g). Significant dark zones with highly deformed shapes can be observed in the pipe. These dark zones are not continuous liquid slugs but highly agitated liquid lumps because there are scattered and non-uniform bright spots inside the dark zones. These frothy liquid lumps are similar to observations in previous studies but with different descriptions.

Sekoguchi and Takeishi (1989) used the term “huge wave” for this lump structure, while Azzopardi and Wren (2004) called these lumps wisps and claimed that the wisps are the same as the huge waves reported by Sekoguchi and Takeishi (1989). Hernandez Perez *et al.* (2010) and Sharaf *et al.* (2016) also used the term “wisps” for these liquid lumps. Later, Parsi *et al.* (2015) described them as a gas/liquid mixture or agitated liquid slugs. These conclusions from published studies are consistent with the dark zones observed in Figs. 3(f) and 3(g). In addition to these frothy lumps, another remarkable interfacial structure is the relatively crumpled liquid film at the rear of the lump. The interfacial structures on the crumpled liquid film exhibit significant downflow, as described in Sec. III C.

Figure 4 is presented to investigate the liquid velocity’s influence on the film reversal. It displays the interfacial structures at a higher superficial liquid velocity of 0.170 m/s. No-FR, Onset-FR, and Complete-FR are again recognized. Compared with Fig. 3, it can be seen that the interfacial structures become much larger at this higher liquid flow rate. In addition, the gas velocity in Fig. 4 separating the No-FR and Onset-FR stages is lower than in Fig. 3. This could be attributed to higher liquid flow rates resulting in more liquid kinetic energy to maintain the upward annular flow. In Figs. 4(f) and 4(g), the size and length of wisps in the Complete-FR stage are significantly larger. From the scale ruler on the pipe wall, the lengths of these wisps are around 50–100 mm, showing agreement with the WMS results of Hernandez Perez *et al.* (2010).

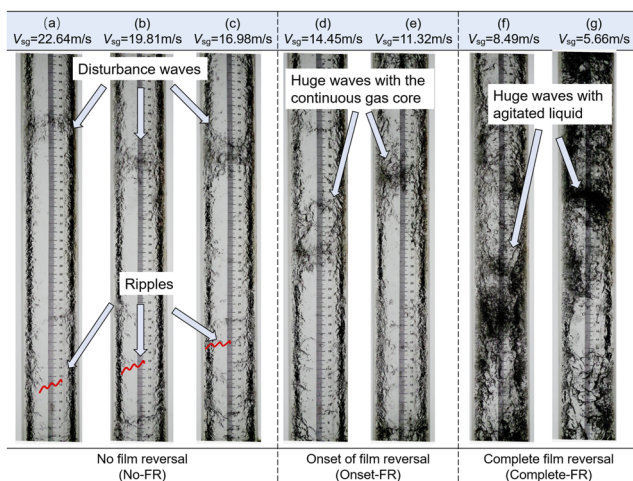


FIG. 3. Visual images at various superficial gas velocities ($V_{sl} = 0.014$ m/s).

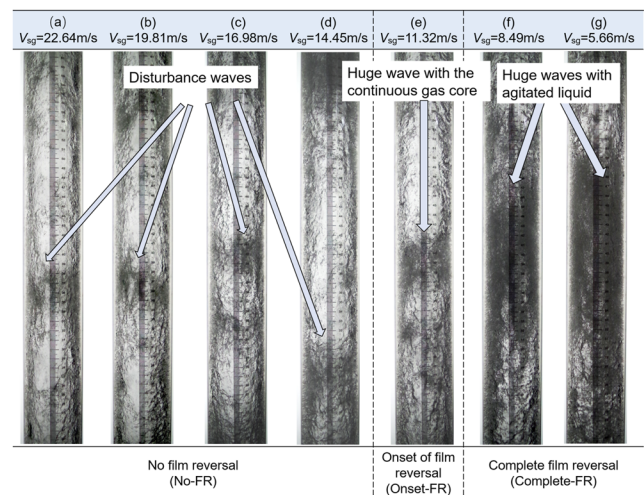


FIG. 4. Visual images at various superficial gas velocities ($V_{sl} = 0.170$ m/s).

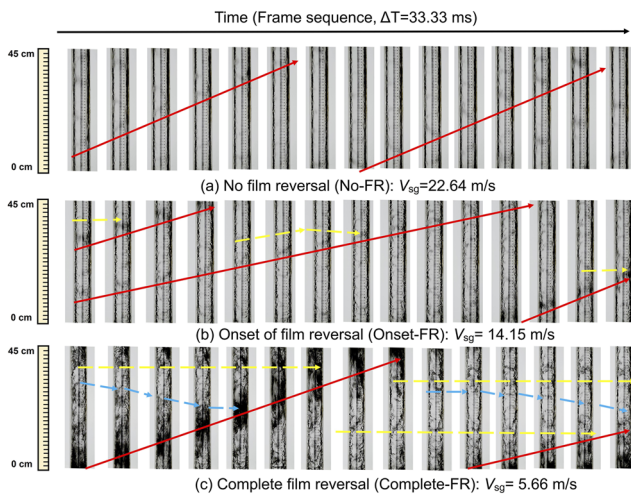


FIG. 5. Video frame sequence of the film reversal ($V_{sl} = 0.014$ m/s). Multimedia view: <https://doi.org/10.1063/5.0135777.1>

C. Trajectories of the interfacial structures

After recognizing the interfacial structures, their trajectories can be captured by the video recordings, as shown in Fig. 5 (multimedia view). Figure 5(a) shows the frame sequence at No-FR (superficial gas velocity = 22.64 m/s). Here, the red arrows highlight the disturbance wave trajectories. It is evident that the disturbance waves flow upward.

The huge waves flow upward when the superficial gas velocity is 14.15 m/s, and Onset-FR happens, but some ripples show stagnant or localized up-down trajectories, as highlighted by the dashed yellow arrows in Fig. 5(b). These stagnant ripples then collide and coalesce with the next huge wave, leading to larger waves that eventually flow upward. These behaviors are identical to the observation of churn flow by Dasgupta *et al.* (2017) and Lin *et al.* (2020).

Figure 5(c) shows Complete-FR when the superficial gas velocity is lowest at 5.66 m/s. The red arrows denote that the wisps flow upward. Then, a relatively crumpled film forms after the wisps have swept upward, and abundant wavy structures appear on the liquid film. These wavy structures can be classified into two forms. One

form is small ripples highlighted by the dotted blue lines in Fig. 5(c). These small ripples show remarkable downflow with an axial displacement, as marked by the dashed blue lines. Then, these falling ripples meet and collide with a huge upward wave, leading to a larger wisp.

The second form looks like a small wisp whose shape is highly deformed and scattered, as marked by the dotted yellow lines in Fig. 5(c). These small wisps are almost stagnant without much downward shift. As time passes, these stagnated small wisps eventually collide and mix with the large upward wisps. Here, an interesting phenomenon is that the dimension of the stagnated small wisp is larger than the falling ripple. One would expect such a larger structure to flow downward violently under gravity, but this visual observation is contradictory.

There are two possible explanations for this phenomenon. The first explanation is that these small wisps are left as disintegrated parts of the large upward wisps. A primary characteristic of the large wisp is its high velocity (Sekoguchi and Takeishi, 1989; Parsi *et al.*, 2015) so that the small wisps disintegrated from the large wisp retain large upward inertia that offsets gravity. A second possible reason could be that a larger wavy structure results in a higher gas velocity in the gas core, so the drag force on the small wisps is more significant than on the ripples. This phenomenon would also keep the small wisps stagnated.

Summarily, based on the visual observation presented above, the criteria to discern the three stages of film reversal are shown in Table I. One could reproduce the film reversal and discriminate the No-FR, Onset-FR, and Complete-FR easily by observing the interfacial structures. It should be noted that although this discrimination procedure relies on visual observation, the recognizing criteria are macroscopic and easy to be observed. The potential uncertainties might be that it is hard to specify a precise value of the transition, which is expected to be minimized by using a high-speed camera to observe the interfacial structures.

D. Tomography using ERT

The tomography visualization results from the ERT are used to investigate the interior structure. In each measuring plane, the ERT can output a series of tomography images at consecutive time steps. In Fig. 6, the tomography results at one moment are presented. Figure 6 shows the tomography images in one measuring plane at

TABLE I. Criteria of recognizing different stages during the film reversal.

Three stages	Interfacial structures	Recognizing criteria
No-FR (no film reversal)	Ripples	Upward motion at high speeds
	Disturbance waves	Upward motion at high speeds
Onset-FR (onset of film reversal)	Stagnated ripples	Stagnating until meet next huge wave
	Huge wave with a continuous gas core	Upward motion at high speeds
Complete-FR (complete film reversal)	Large wisps with gas/liquid mixtures	Upward motion at high speeds
	Falling ripples	Falling until meet next large wisp
	Stagnated small wisps	Stagnating until meet next large wisp

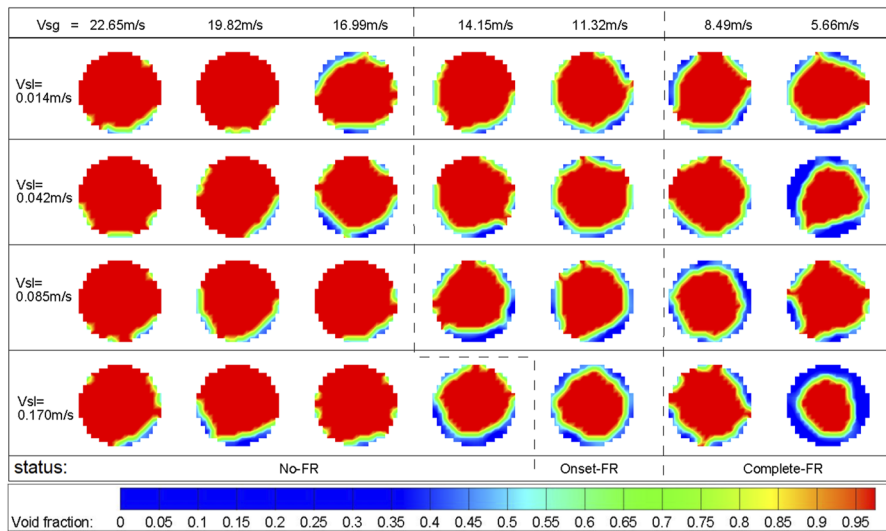


FIG. 6. Tomography results in one measuring plane at various gas and liquid velocities.

various gas and liquid velocities. It should be noted that, the quantity used to represent the interior structure is void fraction. Here, red denotes the high void fraction, i.e., gas phase, while blue denotes the low void fraction, i.e., liquid phase. It can be seen that when the gas velocity is high, and No-FR occurs, there is a thin film in the image. The liquid film becomes thicker when the gas velocity is decreased to Onset-FR. At the Complete-FR stage, the cross-section occupied by the liquid phase is significantly larger.

Figure 7 compares ERT results with visual observations at the superficial liquid velocity of 0.014 m/s. In Figs. 7(a)–7(c), the colorful pictures on the left side are obtained by stacking the time series of tomography images in one measuring plane. Hence, the vertical axis of these colorful pictures is time scale. For the black-and-white pictures at the right side, they are high-resolution photos from the camera. So, the vertical axis of these photos is pipe length scale. Although these ERT images and photos are not synchronized, they are presented together to qualitatively express the agreement between ERT tomography and visual observation.

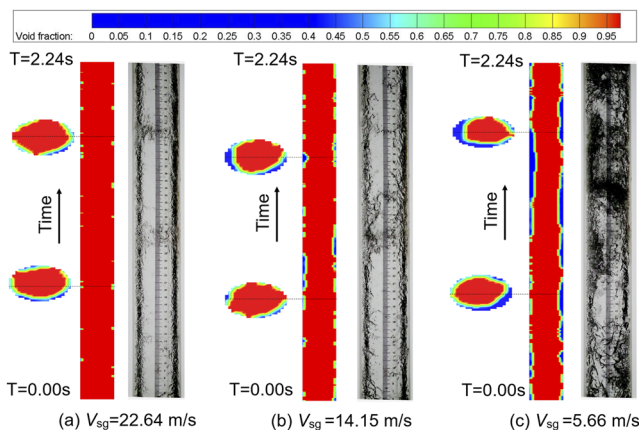


FIG. 7. Comparison of tomography images with visual observation.

It can be seen that, when the gas velocity is 22.64 m/s, and No-FR occurs, the liquid film is fairly thin and uniform, and the captured disturbance waves coincide with the visual photos, as shown in Fig. 7(a). When the gas velocity is decreased to 14.15 m/s, the Onset-FR stage is observed, and Fig. 7(b) indicates that the interfacial wave scale and height increase. When the flow pattern is Complete-FR, as shown in Fig. 7(c), the interfacial waves are captured at a considerable radial distance and a long timescale, corresponding to the wisps of gas–liquid mixture observed by the camera.

However, it should be noted that the interior structure of the wisps cannot be imaged because of the technical limitations of ERT. Because ERT is an electrical resistance technique, it only works when an electrically conducting medium contacts the electrodes, so some droplets in the gas core cannot be imaged. But this does not invalidate the experimental results. In general, the tomography images in Figs. 6 and 7 agree well with the visual photos and expose the typical structures during the evolution with decreasing gas velocity.

E. Analysis of void fractions

The discussion above mainly analyzed the interfacial structures' morphologies, motion trajectories, and tomography images during the evolution process. In this section, the void fractions during the evolution process are analyzed to answer two questions: How do the void fractions evolve during the film reversal? Could one recognize the three stages from the void fractions?

1. Mean void fraction and error analysis

Before analyzing the void fraction quantitatively, it is important to examine the experimental repeatability and reliability. Hence, we conducted multiple tests to calculate the mean void fraction in this subsection.

Firstly, the time-averaged void fraction for each test was calculated. Then, the mean void fraction was calculated based on the time-averaged void fraction of each test, as presented in Eq. (1). Besides, standard deviation (STD) and relative standard deviation (RSD) were calculated using Eqs. (2) and (3),

$$\bar{\alpha} = \frac{1}{N} \sum_{i=1}^N \alpha_i, \tag{1}$$

$$STD = \sqrt{\frac{1}{N} \sum_{i=1}^N (\alpha_i - \bar{\alpha})^2}, \tag{2}$$

$$RSD = \frac{STD}{\bar{\alpha}}, \tag{3}$$

where α_i is the time-averaged void fraction at one test, $\bar{\alpha}$ is the mean void fraction of multiple tests, N is the number of experiments, STD is the standard deviation of multiple tests, and RSD is the relative standard deviation of multiple tests.

The symbols in Fig. 8 are the mean void fractions, and the error bars are the standard deviations from multiple experiments. The standard deviation ranges from 1.83×10^{-3} to 2.19×10^{-2} , and the relative standard deviation ranges from 0.19% to 2.62%. These statistical parameters demonstrate the current experiment's repeatability.

The experimental accuracy was evaluated by comparing the mean void fractions with previous models. Woldesemayat and Ghajar (2007) developed a modified correlation to predict the void fraction in vertical, inclined, and horizontal pipes based on extensive experimental datasets. They concluded that this improved correlation is outperformed compared with other prediction models. Minami and Brill (1987) proposed an empirical correlation for the void fraction in horizontal pipes to cover the entire range of liquid holdup. These two correlations from Woldesemayat and Ghajar (2007) and Minami and Brill (1987) were adopted here. The comparison results are shown in Fig. 9.

It can be seen that the estimated void fractions from the model of Minami and Brill (1987) are higher than the mean void fractions from the experiment, which could be attributed to that of Minami and Brill (1987) was developed for horizontal pipe while the current experiments were conducted in a vertical pipe. The void fractions estimated by Woldesemayat and Ghajar (2007) are slightly smaller

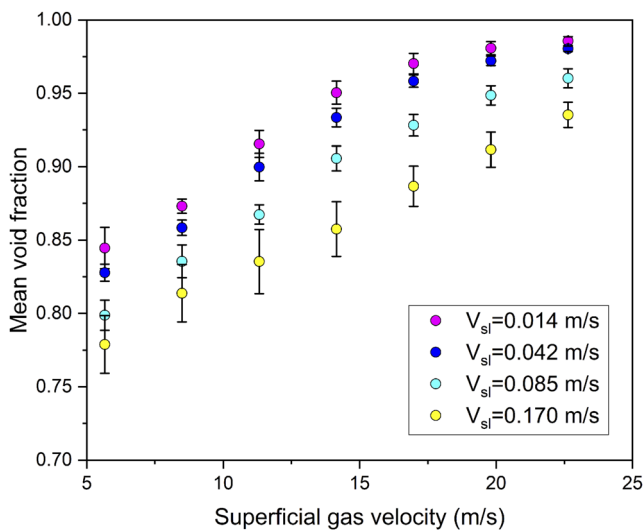


FIG. 8. Mean void fraction of multiple tests.

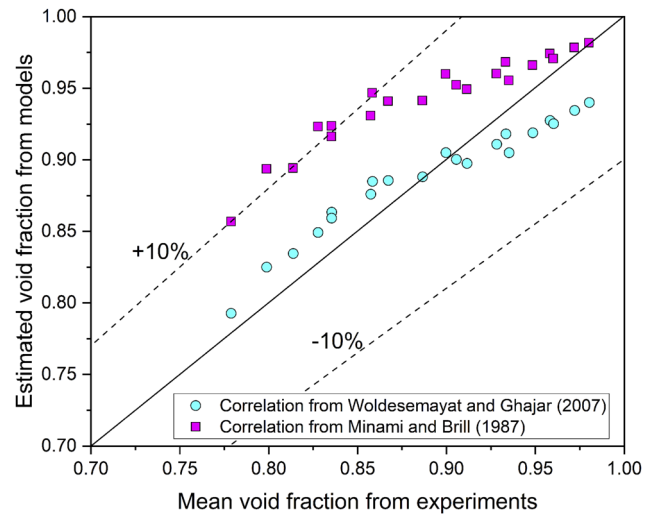


FIG. 9. Comparison between mean void fraction from experiments and estimated void fraction from correlations.

than the mean value in the experiment when the void fraction is >0.90 . This could be caused by that more droplets were generated under the condition of high void fraction, but they cannot be detected by the ERT. As for the low void fraction conditions, predictions by Woldesemayat and Ghajar (2007) are slightly higher than the mean value from experiments. This could be attributed by that there are too much gas/liquid mixture, so that ERT would recognize gas phase as liquid phase in the mixture. Although some uncertainties exist in the experiment, it can be seen that the majority of the symbols are close to the diagonal, and the relative errors are $<10\%$.

It should be noted that the uncertainties of multiple tests could be propagated to relative errors (Bevington and Robinson, 2003), so error propagation is considered. The results show that when error propagation is introduced, the absolute relative error ranges from 0.30% to 13.23%. Overall, these errors are acceptable and verify the accuracy of the current approach.

2. Time series of void fraction

The statistical void fraction from multiple tests has been investigated to clarify experimental repeatability and accuracy. Then, in this subsection, the time series of void fraction in one experiment will be analyzed to study the evolution characteristic of void fraction during the film reversal.

Figures 10(a)–10(d) display the void fraction at four superficial liquid velocities. In each graph, the green, blue, and red lines denote the No-FR, Onset-FR, and Complete-FR stages, respectively.

The green lines show that when superficial gas velocity is high, and the flow pattern is No-FR, the time series exhibit small regular oscillations caused by the periodic disturbance waves, so the void fraction is relatively stable in No-FR. When the gas velocity is decreased to Onset-FR, the blue lines indicate that the void fraction oscillations are stronger, implying the occurrence of huge waves with the continuous gas core. The red lines show remarkable vibrations for Complete-FR when decreasing gas velocity further. This change can be attributed to the alternating appearance of wispy structures,

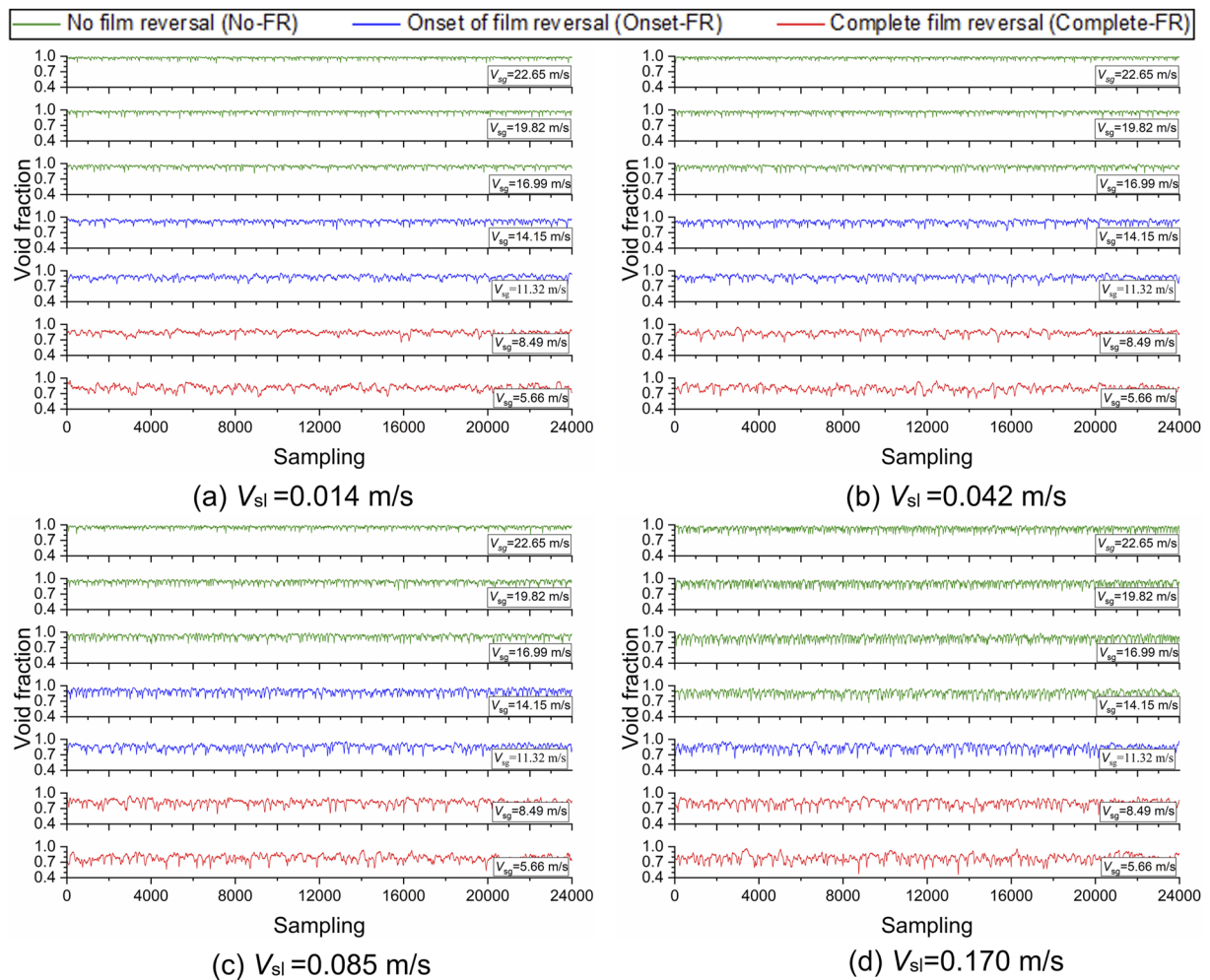


FIG. 10. Void fraction time series at various gas and liquid velocities.

small wisps, and small ripples on the wrinkled falling film, as shown in Figs. 4 and 5.

The average (AVE) and standard deviation (STD) values of the time series are presented in Fig. 11. As distinguished by the dotted lines, Fig. 11 indicates that the No-FR, Onset-FR, and Complete-FR stages occur successively with decreasing gas velocity. It should be noted that these dotted lines do not strictly specify the boundaries of the three flow stages but are used to distinguish them qualitatively. In Fig. 11(a), it is clear that the average void fraction exhibits a monotonic decrease with decreasing gas velocity. On the contrary, Fig. 11(b) shows that the standard deviation increases monotonically, indicating that the void fraction oscillations increase markedly.

An important feature of Fig. 11 is that the differences in the AVE and STD values between No-FR and Complete-FR are relatively large. However, the changing tendency from No-FR to Complete-FR is almost linear and smooth. Each curve's slope is relatively gentle, and no sudden changes or singular points occur. This

could be attributed to the Onset-FR stage, located between No-FR and Complete-FR, causing this smooth transition and verifying that the flow regime transition is a gradual process. However, this gradual tendency also leads to the conclusion that it is difficult to recognize when flow regime transition happens from the AVE and STD of the void fraction alone.

3. Probability density function (PDF)

The void fraction's probability density function (PDF) provides a statistical method to determine the flow pattern (Kajero *et al.*, 2018). Figures 12(a)–12(d) presents PDF curves at various superficial liquid velocities, with arrows marking the three flow stages.

No-FR occurs when the superficial gas velocities are 22.65, 19.82, and 16.99 m/s, and the corresponding PDF curves exhibit steep slopes with a single sharp peak. These are typical characteristics of annular flow. By contrast, the PDF curves of Complete-FR exhibit different distinctive features. It can be seen from Fig. 12 that the PDF curve for Complete-FR has gentle slopes and a sin-

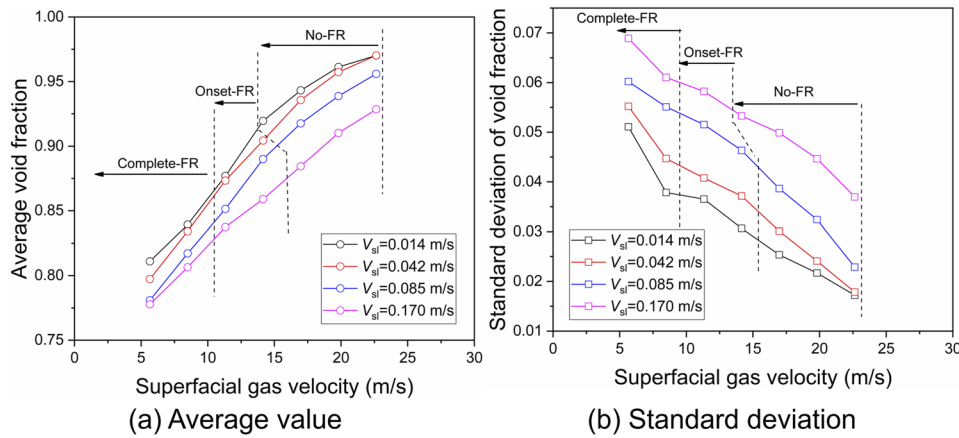


FIG. 11. Average (AVE) and standard deviation (STD) values of the void fraction.

gle peak that flattens with increasing liquid velocity. This demonstrates that more wisps exist at various void fractions, and their occurrence probability is relatively scattered. These characteristics agree with the PDF curves in churn flow reported by *Parsi et al. (2015)*.

Between No-FR and Complete-FR, the PDF curves of Onset-FR have intermediate characteristics. Specifically, Onset-FR's PDF curves have a single sharp peak similar to No-FR, as well as

gentle slopes similar to Complete-FR, implying that the void fraction of Onset-FR has both No-FR and Complete-FR characteristics. It is then reasonable to conclude that Onset-FR plays a transition role between No-FR and Complete-FR. This provides additional strong evidence that the flow pattern's evolution is gradual.

According to the characteristics of the PDF curves, it is feasible to recognize No-FR and Complete-FR because they exhibit distinct features. However, considering the gradual evolution, it is still

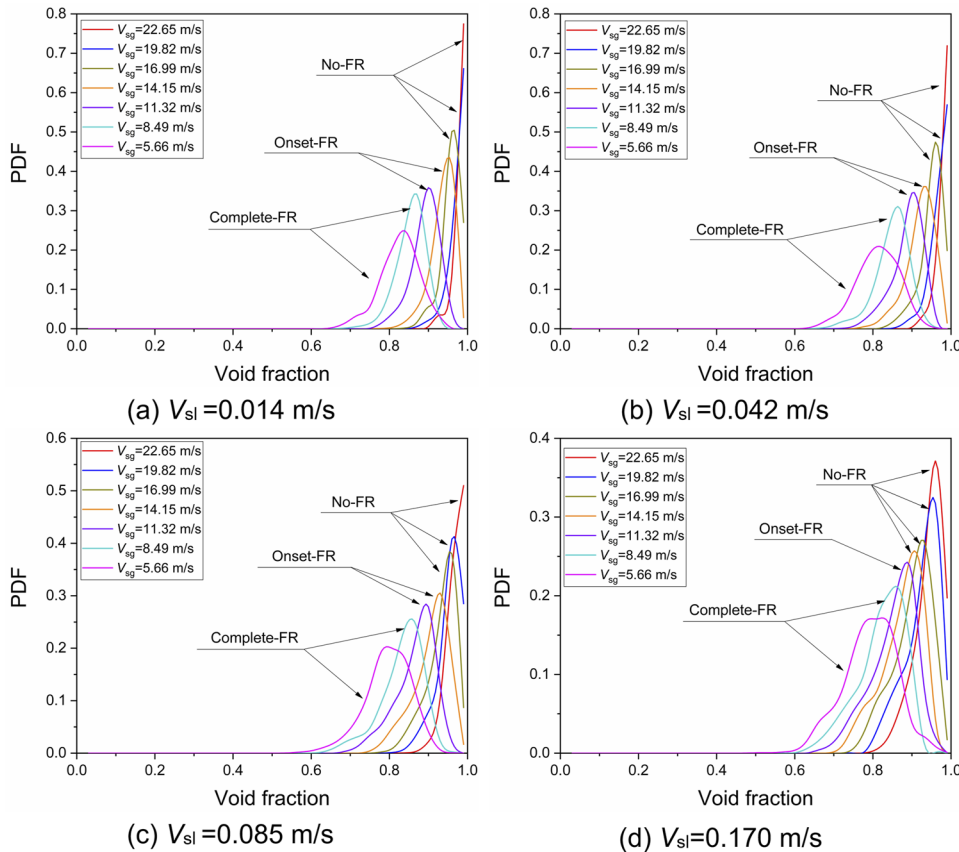


FIG. 12. PDFs of the void fractions at various gas and liquid velocities.

08 April 2024 03:16:44

insufficient to identify clear transition boundaries between No-FR, Onset-FR, and Complete-FR.

4. Power spectral density (PSD)

A powerful alternative technique to identify the flow state is frequency domain analysis. Here, the fast Fourier transform (FFT) is used to convert the void fraction's time domain to the frequency domain. The power spectral density (PSD) of the void fraction is displayed in Fig. 13, where the green, blue, and red lines are No-FR, Onset-FR, and Complete-FR, respectively. It can be seen that the frequency band mainly spreads in the range from 0 to 20 Hz, and the dominant frequency band shifts from large to small with decreasing gas velocity in each graph.

The green lines show that frequency curves' peak values and amplitudes are relatively small in No-FR, meaning that the annular flow is stable without much disturbance, corresponding to a steady and continuous liquid film and gas core flow. When the flow pattern is Onset-FR, the PSD's peaks in the blue lines are larger, and the variation in the PSD curves is greater. The red PSD curves exhibit remarkably high peaks and significant oscillation for Complete-FR.

Figure 14 presents the AVE and STD values of the PSD curves. The AVE and STD increase monotonically as the flow changes from No-FR to Complete-FR. The differences between No-FR and Complete-FR are remarkable. However, the changing tendencies of the two statistical parameters are moderate and gradual without sharp changes, as in Fig. 11. Hence, as discussed previously for Fig. 11, these monotonic tendencies demonstrate that the Onset-FR stage has characteristics of the No-FR and Complete-FR stages, and the film reversal is a gradual process.

F. Comparisons with published studies

1. Comparison with published datasets

The effects of pipe size and liquid velocity on the evolution process are examined by comparing the current experimental results with the datasets of Dasgupta *et al.* (2017) and Lin *et al.* (2020), as shown in Fig. 15. Dasgupta *et al.* (2017) studied the dominant waves in an 11 mm vertical pipe, reporting annular, pre-annular, and churn flow. They found that the ripples stagnated in pre-annular flow. Lin *et al.* (2020) conducted experiments for annular flow in a 20 mm pipe and analyzed the interfacial waves. They also observed

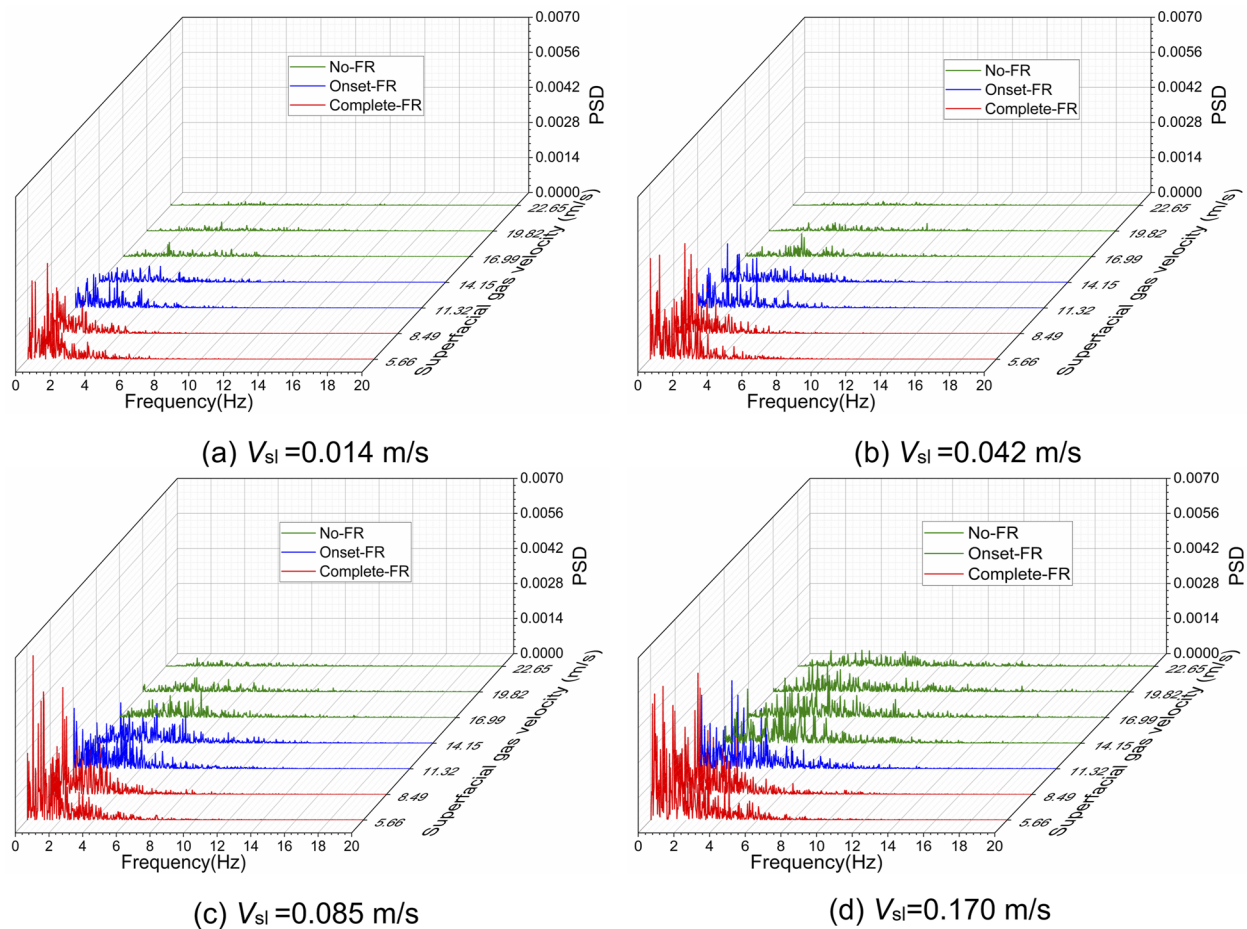


FIG. 13. PSDs of the void fractions at various gas and liquid velocities.

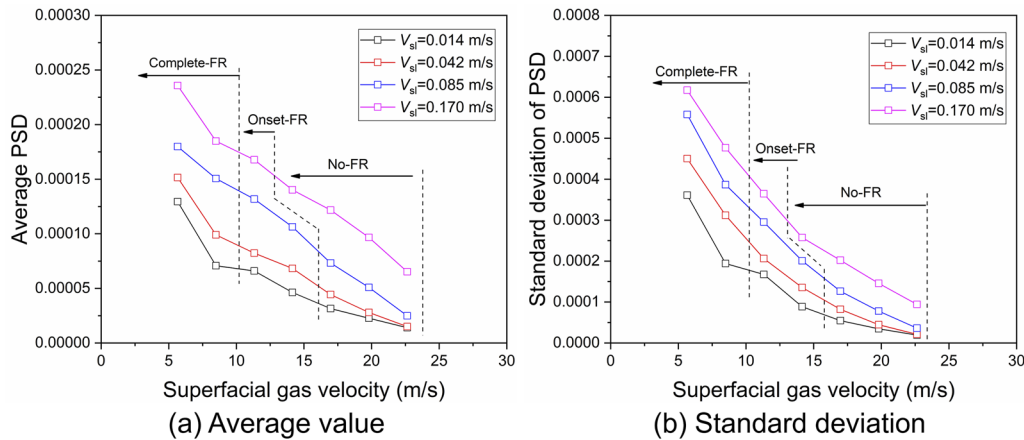


FIG. 14. Average (AVE) and standard deviation (STD) values of the PSDs.

stagnated ripples and recognized them as churn flow. Figure 15 plots these datasets on the Hewitt and Robert (1969) flow map. In Fig. 15, the green points represent No-FR (annular flow). The yellow points are Onset-FR, indicating that stagnated ripples were observed, and the red points denote Complete-FR (churn flow).

Figure 15 shows that the current experiments are consistent with the published datasets. Boundaries can be found to discriminate No-FR, Onset-FR, and Complete-FR. The dotted blue lines mark a prominent band for the Onset-FR stage. It covers the data points where stagnated ripples were observed in current and previous experiments. It can be seen that this band is slightly above the boundary between annular and churn flow. This is reasonable because Onset-FR could be prone to be recognized as an annular

flow, considering their morphologies are similar. The width of this band appears to be insensitive to the pipe diameter. The band narrows and shifts to lower gas velocities with increasing liquid velocity, coinciding with the results in Fig. 5. It would be expected that the Onset-FR stage would disappear if the liquid velocity was increased further. This is reasonable because the flow regime would change from wispy-annular flow to churn flow directly if there is a large amount of entrained liquid at high liquid flow rates.

2. Comparison with existing transition correlations

The comparison with published datasets showed that the observed film reversal is closely related to the flow regime transition between annular flow and churn flow. This subsection compares the current work with existing correlations for the transition between annular and churn flow.

Various models have been proposed in the past to predict the transition between annular and churn flow. With the flooding mechanism, McQuillan and Whalley (1985) used Eq. (4) as the transition criterion between churn and annular flow,

$$V_{sg} \sqrt{\frac{\rho_g}{gD(\rho_l - \rho_g)}} \geq 1, \tag{4}$$

where V_{sg} is the superficial gas velocity (m/s), g is the gravitational acceleration (9.81 m/s^2), ρ_l is the liquid density (kg/m^3), ρ_g is the gas density (kg/m^3), and D is the pipe diameter (m).

Taitel et al. (1980) proposed a mechanistic model as the transition criteria between annular and churn flow based on postulated droplet reversal. The correlation Eq. (5) was developed using a force balance analysis, where σ is the surface tension (N/m),

$$V_{sg} = 3.1 \left[\frac{\sigma g (\rho_l - \rho_g)}{\rho_g^2} \right]^2. \tag{5}$$

Mishima and Ishii (1984) predicted the transition between churn and annular flow according to two mechanisms. The first mechanism is liquid film reversal along with large bubbles, as given

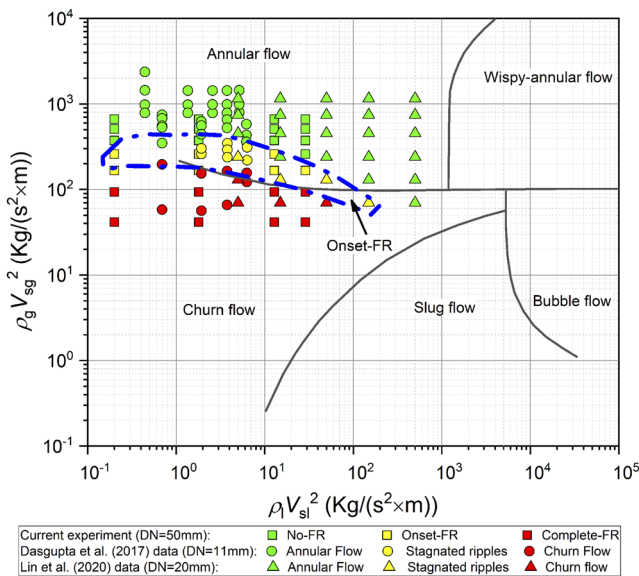


FIG. 15. Comparison between current data and published datasets.

by Eq. (6). The second criterion is based on the mechanism of droplet entrainment inception, as in Eq. (7),

$$V_{sg} = \sqrt{\frac{gD(\rho_l - \rho_g)}{\rho_g}(\alpha - 0.11)}, \quad (6)$$

$$V_{sg} \geq N_{\mu l}^{-0.2} \left(\frac{\sigma g(\rho_l - \rho_g)}{\rho_g^2} \right)^{1/4}, \quad (7)$$

where

$$N_{\mu l} = \frac{\mu_l}{(\rho_l \sigma \sqrt{\sigma/g(\rho_l - \rho_g)})^{1/2}}, \quad (8)$$

where μ_l is the liquid viscosity (mPa s), and α is the void fraction, which can be calculated by the relationship from drift-flux model (Mishima and Ishii, 1984).

Barnea (1986) proposed a mechanistic model to predict the critical gas velocity from annular to churn flow using a force balance on the liquid film. A stability analysis was adopted to determine the critical transition condition (Taitel et al., 1982; Barnea, 1986). In our previous work (Wang et al., 2022), an improved model was proposed by considering the liquid film's interior viscosity and velocity distribution. The specific formulations and solution procedures for these film reversal models can be found in Wang et al. (2022).

Figure 16 plots the flow regime points and existing transition correlations. It can be observed that models of Barnea (1986), McQuillan and Whalley (1985), and Wang et al. (2022) overestimate the occurrence of Onset-FR. The Taitel et al. (1980) and Mishima and Ishii (1984) models are excellent at predicting the gas velocities at which Onset-FR occurs. This matches the evaluation results of Wu et al. (2017), in which the Taitel et al. (1980) and Mishima and Ishii (1984) correlations exhibited high accuracy in estimating the transition from annular to churn flow. This also verifies the reasonableness of treating the Onset-FR stage as a churn flow.

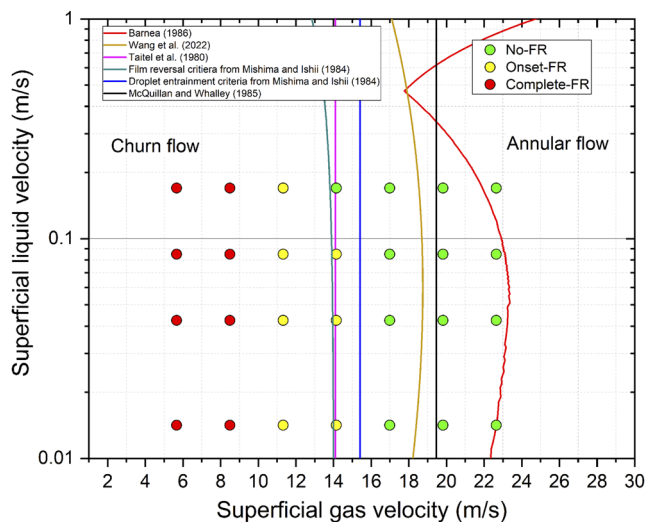


FIG. 16. Comparison between current data and existing correlations.

The excellent performance of these steady-state mechanistic models in Fig. 16 also implies that steady models can describe the Onset-FR stage. In particular, considering that the Onset-FR morphology is similar to annular flow, some annular flow modeling approaches could be expanded to Onset-FR. This result is similar to the conclusion of Waltrich et al. (2015), who studied the transition from annular to churn flow in a long vertical pipe and suggested that steady-state models could be used. These findings provide guidance for establishing future film reversal or interfacial wave models.

IV. CONCLUSIONS

Laboratory experiments have been conducted in a vertical 50-mm-diameter pipe to study film reversal evolution characteristics. Interfacial structures, motion trajectories, and void fractions have been analyzed, and the results are consistent with published studies. The findings in this work contribute to understanding the evolution process and establishing mechanistic film reversal models. The main conclusions are summarized below.

New criteria have been proposed to objectively classify the film reversal into no film reversal (No-FR), onset of film reversal (Onset-FR), and complete film reversal (Complete-FR). When the gas velocity is relatively high, No-FR occurs, and its typical morphology is a continuous liquid film and gas core. Because of the high gas velocity, disturbance waves and ripples flow upward.

Onset-FR occurs with a decrease in gas velocity. Like No-FR, the Onset-FR morphology consists of a continuous gas core and liquid film, but there are stagnated ripples on the gas-liquid interface. The stagnant ripples eventually meet and collide with huge upward waves. Here, the huge wave in Onset-FR coincides with the "huge wave with a continuous gas core" described by Parsi et al. (2015).

A further decrease in the gas velocity results in the Complete-FR stage. This flow pattern can be recognized when upward wisps occur as chaotic gas-liquid mixtures observed as highly deformed dark zones in the transparent pipe. The occurrence of these wisps increases with decreasing gas velocity, consistent with the studies of Azzopardi and Wren (2004), Hernandez Perez et al. (2010), Sharaf et al. (2016), and Parsi et al. (2015). There is a relatively wrinkled liquid film with two interfacial structures in the domain where upward wisps have swept past. One structure is falling ripples, and another is stagnated small wisps left as disintegrated parts of upward wisps. Eventually, these structures collide with upward wisps. Generally, the upward wisps and wrinkled films alternate, resulting in relatively churned and frothy phenomena.

The void fractions have been analyzed in the time and frequency domains. The AVE, PDF, and STD statistical parameters exhibit clear differences between No-FR and Complete-FR, showing the features of annular and churn flow, respectively. Onset-FR shows intermediate characteristics because its characteristics are similar to both No-FR and Complete-FR, resulting in a gradually evolving film reversal without sudden changes. This finding implies that it would be difficult to determine strict transition boundaries among No-FR, Onset-FR, and Complete-FR using only these statistical parameters.

A comparison with other published datasets shows that the Onset-FR stage would disappear if the liquid velocity is relatively large because the flow regime may change from wispy-annular flow to churn flow directly with a large amount of entrained liquid phase.

In addition, the successful application of steady mechanistic models suggests that it may be possible to use steady models to describe Onset-FR, especially considering that Onset-FR consists of a regular, continuous gas core and liquid film.

ACKNOWLEDGMENTS

This work was financially supported by the National Natural Science Foundation of China (Grant No. 51779243), the Strategic Priority Research Program of the Chinese Academy of Science (Grant No. XDB22030101), and the National Natural Science Foundation of China Youth Fund Project (Grant No. 12102436).

AUTHOR DECLARATIONS

Conflict of Interest

The authors have no conflicts to disclose.

Author Contributions

Lisong Wang: Conceptualization (lead); Methodology (lead); Validation (equal); Writing – original draft (equal). **Meng Yang:** Investigation (equal); Resources (equal); Visualization (equal). **Lintong Hou:** Data curation (equal); Investigation (equal); Visualization (equal). **Shuo Liu:** Conceptualization (equal); Project administration (equal); Resources (equal); Supervision (equal). **Jian Zhang:** Investigation (equal); Methodology (equal); Resources (equal). **Jing-yu Xu:** Conceptualization (equal); Funding acquisition (lead); Project administration (lead); Supervision (lead).

DATA AVAILABILITY

The data that support the findings of this study are available from the corresponding authors upon reasonable request.

REFERENCES

- Alekseenko, S., Antipin, V., Cherdantsev, A., Kharlamov, S., and Markovich, D., “Two-wave structure of liquid film and wave interrelation in annular gas-liquid flow with and without entrainment,” *Phys. Fluids* **21**, 061701 (2009).
- Azzopardi, B. J. and Wren, E., “What is entrainment in vertical two-phase churn flow?,” *Int. J. Multiphase Flow* **30**, 89–103 (2004).
- Barbosa, J. R., Ferreira, J. C. A., and Hense, D., “Onset of flow reversal in upflow condensation in an inclinable tube,” *Exp. Therm. Fluid Sci.* **77**, 55–70 (2016).
- Barnea, D., “Transition from annular flow and from dispersed bubble flow—Unified models for the whole range of pipe inclinations,” *Int. J. Multiphase Flow* **12**, 733–744 (1986).
- Belfroid, S. P. C., Schiferli, W., Alberts, G. J. N., Veeken, C. A. M., and Biezen, E., “Prediction onset and dynamic behaviour of liquid loading gas wells,” in *SPE Annual Technical Conference and Exhibition* (Society of Petroleum Engineers, 2008).
- Bevington, P. and Robinson, D. K., *Data Reduction and Error Analysis for the Physical Sciences* (McGraw-Hill Education, 2003).
- Coleman, S. B., Clay, H. B., McCurdy, D. G., and Norris, L. H., “A new look at predicting gas-well load-up,” *J. Pet. Technol.* **43**, 329–333 (1991).
- Dasgupta, A., Chandraker, D. K., Kshirasagar, S., Reddy, B. R., Rajalakshmi, R., Nayak, A. K., Walker, S. P., Vijayan, P. K., and Hewitt, G. F., “Experimental investigation on dominant waves in upward air-water two-phase flow in churn and annular regime,” *Exp. Therm. Fluid Sci.* **81**, 147–163 (2017).
- Govan, A. H., Hewitt, G. F., Richter, H. J., and Scott, A., “Flooding and churn flow in vertical pipes,” *Int. J. Multiphase Flow* **17**, 27–44 (1991).
- Guner, M., Pereyra, E., Sarica, C., and Torres, C., “An experimental study of low liquid loading in inclined pipes from 90° to 45°,” in *SPE Production and Operations Symposium* (Society of Petroleum Engineers, 2015).
- Guo, B., Ghalambor, A., and Xu, C., “A systematic approach to predicting liquid loading in gas wells,” *SPE Prod. Oper.* **21**(01), 81–88 (2006).
- Hernandez Perez, V., Azzopardi, B. J., Kaji, R., da Silva, M. J., Beyer, M., and Hampel, U., “Wisp-like structures in vertical gas-liquid pipe flow revealed by wire mesh sensor studies,” *Int. J. Multiphase Flow* **36**, 908–915 (2010).
- Hewitt, G. F., “Experimental and modelling studies of annular flow in the region between flow reversal and the pressure drop minimum,” *Phys.-Chem. Hydrodyn.* **6**, 43–50 (1985).
- Hewitt, G. F. and Hall-Taylor, N. S., *Annular Two-Phase Flow* (Pergamon, Amsterdam, 1970), pp. 4–20.
- Hewitt, G. F. and Roberts, D. N., “Studies of two-phase flow patterns by simultaneous x-ray and fast photography” (n.d.) Technical Report AERE-M-2159, Atomic Energy Research Establishment (1969).
- Jia, J., Wang, M., Schlager, H. I., and Li, H., “A novel tomographic sensing system for high electrically conductive multiphase flow measurement,” *Flow Meas. Instrum.* **21**, 184–190 (2010).
- Kajero, O. T., Abdulkadir, M., Abdulkareem, L., and Azzopardi, B. J., “Experimental study of viscous effects on flow pattern and bubble behavior in small diameter bubble column,” *Phys. Fluids* **30**, 093101 (2018).
- Kumar, P., Das, A. K., and Mitra, S. K., “Physical understanding of gas-liquid annular flow and its transition to dispersed droplets,” *Phys. Fluids* **28**, 072101 (2016).
- Lin, R., Wang, K., Liu, L., Zhang, Y., and Dong, S., “Study on the characteristics of interfacial waves in annular flow by image analysis,” *Chem. Eng. Sci.* **212**, 115336 (2020).
- Liu, S., Zhang, J., and Xu J.-Y., “An investigation of a gas-liquid swirling flow with shear-thinning power-law liquids,” *Phys. Fluids* **34**, 073320 (2022).
- Luan, T. N. and Vemuri, B., “Modeling and experimental studies of wave evolution on free falling viscous films,” *Phys. Fluids* **12**, 2236 (2000).
- Luo, S., Kelkar, M., Pereyra, E., and Sarica, C., “A new comprehensive model for predicting liquid loading in gas wells,” *SPE Prod. Oper.* **29**, 337–349 (2014).
- McQuillan, K. W. and Whalley, P. B., “Flow patterns in vertical two-phase flow,” *Int. J. Multiphase Flow* **11**, 161–175 (1985).
- Minami, K. and Brill, J. P., “Liquid holdup in wet-gas pipelines,” *SPE Prod. Eng.* **2**, 36–44 (1987).
- Mishima, K. and Ishii, M., “Flow regime transition criteria for upward two-phase flow in vertical tubes,” *Int. J. Heat Mass Transfer* **27**, 723–737 (1984).
- Nosseir, M. A., Darwich, T. A., Sayyouh, M. H., and Sallaly, M. E. I., “A new approach for accurate prediction of loading in gas wells under different flowing conditions,” in *SPE Production Operations Symposium* (Society of Petroleum Engineers, 2000).
- Park, I. and Mudawar, I., “Climbing film, flooding and falling film behavior in upflow condensation in tubes,” *Int. J. Heat Mass Transfer* **65**, 44–61 (2013).
- Parsi, M., Vieira, R. E., Torres, C. F., Kesana, N. R., McLaury, B. S., Shirazi, S. A., Schleicher, E., and Hampel, U., “Experimental investigation of interfacial structures within churn flow using a dual wire-mesh sensor,” *Int. J. Multiphase Flow* **73**, 155–170 (2015).
- Pushkina, O. L. and Sorokin, Y. L., “Breakdown of liquid film motion in vertical tubes,” *Heat Transfer-Sov. Res.* **1** (5), 56–64 (1969).
- Sekoguchi, K. and Takeishi, M., “Interfacial structures in upward huge wave flow and annular flow regimes,” *Int. J. Multiphase Flow* **15**, 295–305 (1989).
- Sharaf, S., van der Meulen, G. P., Agunlejika, E. O., and Azzopardi, B. J., “Structures in gas-liquid churn flow in a large diameter vertical pipe,” *Int. J. Multiphase Flow* **78**, 88–103 (2016).
- Taitel, Y., Barnea, D., and Dukler, A. E., “A film model for the prediction of flooding and flow reversal for gas-liquid flow in vertical tubes,” *Int. J. Multiphase Flow* **8**, 1–10 (1982).

- Taitel, Y., Barnea, D., and Dukler, A. E., "Modelling flow pattern transitions for steady upward gas-liquid flow in vertical tubes," *AIChE J.* **26**, 345–354 (1980).
- Turner, R. G., Hubbard, M. G., and Dukler, A. E., "Analysis and prediction of minimum flow rate for the continuous removal of liquids from gas wells," *J. Pet. Technol.* **21**, 1475–1482 (1969).
- van 't Westende, J. M. C., Kemp, H. K., Belt, R. J., Portela, L. M., Mudde, R. F., and Oliemans, R. V. A., "On the role of droplets in cocurrent annular and churn-annular pipe flow," *Int. J. Multiphase Flow* **33**, 595–615 (2007).
- Veeken, C. A. M., Hu, B., and Schiferli, W., "Transient multiphase flow modeling of gas well liquid loading," in *Offshore Europe* (Society of Petroleum Engineers, 2009).
- Wallis, G. B., *One Dimensional Two-Phase Flow* (McGraw-Hill, 1969).
- Wallis, G. B. and Makkenchery, S., "The hanging film phenomenon in vertical annular two-phase flow," *J. Fluids Eng.* **96**, 297–298 (1974).
- Waltrich, P. J., Falcone, G., and Barbosa, J. R., "Liquid transport during gas flow transients applied to liquid loading in long vertical pipes," *Exp. Therm. Fluid Sci.* **68**, 652–662 (2015).
- Wang, G., Dang, Z., and Ishii, M., "Wave structure and velocity in vertical upward annular two-phase flow," *Exp. Therm. Fluid Sci.* **120**, 110205 (2021).
- Wang, L.-s., Liu, S., Hou, L.-t., Yang, M., Zhang, J., and Xu, J.-y., "Prediction of the liquid film reversal of annular flow in vertical and inclined pipes," *Int. J. Multiphase Flow* **146**, 103853 (2022).
- Wang, M., "Electrical impedance tomography," in *Industrial Tomography: Systems and Applications* (Elsevier, 2015).
- Woldesemayat, M. A. and Ghajar, A. J., "Comparison of void fraction correlations for different flow patterns in horizontal and upward inclined pipes," *Int. J. Multiphase Flow* **33**, 347–370 (2007).
- Wu, B., Firouzi, M., Mitchell, T., Rufford, T. E., Leonardi, C., and Towler, B., "A critical review of flow maps for gas-liquid flows in vertical pipes and annuli," *Chem. Eng. J.* **326**, 350–377 (2017).